
Effects on cavitation inception of leading and trailing edge flaps on a high-performance hydrofoil

Mohammed Arab Fatiha ¹, Augier Benoit ², Deniset François ¹, Casari Pascal ³,
Astolfi Jacques André ^{1,*}

¹ French Naval Academy Research Institute (IRENav), EA 3634, 29240 Brest, France

² IFREMER, RDT, F-29280 Plouzané, France

³ Research Institute in Civil Engineering and Mechanics—GeM, 44606 Saint-Nazaire, France

* Corresponding author : Jacques André Astolfi, email address : jacques-andre.astolfi@ecole-navale.fr

Abstract :

For high-performance foiling yachts, cavitation is often a limiting factor for take-off and top speed. The present work investigates solutions to control the onset of cavitation thanks to a combination of leading edge and trailing edge flaps. Numerical and experiments in a hydrodynamic tunnel are conducted in order to assess the effect of specific geometric parameters on the hydrodynamic performance and cavitation inception. The hydrofoils are manufactured using an additive 3D printing technique and tested in the cavitation tunnel of IRENav at an inflow velocity of (). The effect on the hydrodynamic performances and cavitation buckets of a 70% chord trailing edge flap and a 20% chord leading edge flap of NACA 0012 is investigated. The results show that the lift coefficient increases and the cavitation bucket shifts up and decreases with the flaps deflection. The experimental results are in good agreement with the numerical ones by highlighting the capacity of the flaps to modify both the operating domain and the cavitation bucket of the hydrofoil. Eventually, the PLA 3D printed foils prove to be a fast, unexpensive and reliable technologies for cavitation studies.

Keywords : Hydrofoil, High performance, Morphing, Cavitation, Flaps

1. Introduction

If new hydrofoil technologies used on sailing boats are intended to improve the hydrodynamic forces, cavitation is often a limiting factor for take-off and top speed.

Using this new concept of hydrofoils allow the control of the lift and drag forces for various operating conditions, but it can lead to cavitation onset at high speed and moderate angles of incidence but also at low speed and high angles. Improving the hydrodynamic performances and delaying the cavitation inception requires the modification of shape, hence the idea of using morphing hydrofoils. Morphing structures could be an interesting way to adapt the performance to different operating regimes ([27]).

The use of morphing structures is particularly considered in aerodynamic applications including flying performance [6]. Jawahar et al. [17] analyzed experimentally and numerically the effect of camber flaps on the pressure distribution, on the lift and drag forces as well as the effect on the wake flow. They concluded that the camber of flaps significantly affects the aerodynamic performance and the downstream wake development of the airfoil. The increase of the camber flap profiles increases the lift coefficients and reduces the lift-to-drag ratio. The aerodynamic performance and mechanical properties of a flexible suction side of an airfoil powered by two actuators are numerically investigated by Brailovski et al. [5].

The gap present at the spanwise ends of the control surfaces is one of the sources of noise and drag. Woods et al. [28] have replaced this gap by a smooth, three-dimensional morphing transition section that elastically lofts between the


rigid wing and the moving control surface in a passive and continuous manner. The passive control of this compliant morphing flap transition has the advantage of increasing the lift and reducing the drag. The effect of various variable camber continuous trailing edge flap (VCCTEF) on the lift and drag forces is discussed by Kaul et al. [18]. It was noted that the best stall performance (L/D) was demonstrated by the circular and parabolic arc camber flaps. In a review, Barbarino et al. summarized shape-changing technologies for fixed and rotary wings and highlighted the need for further research on skins, actuators/mechanisms and control theories ([4]).

Most objectives of hydrodynamic applications are similar to those of aerodynamics. The airfoil technology can be then used in the design of the hydrofoil by taking the differences between the fluid properties and the cavitation phenomena into account .

To meet hydrodynamic requirements, adaptive composites are used in many marine technologies including propulsive devices, underwater vehicles and propellers. In [29], the authors summarized the progress on the numerical modeling, the experimental studies, design and optimization of adaptive composite marine propulsors and turbines.

In order to assess the effect of cavitation on the structural response, Ducoin et al. [9] have studied the displacement of a flexible homogeneous POM hydrofoil in a cavitating flow. They found that the hydrodynamic loading unsteadiness increases vibrations experienced by the hydrofoil. Numerically, Garg et al. ([11], [12], [13]) have developed a shape optimization tool to predict the hydrodynamic performance including cavitation inception conditions. The predicted hydrodynamic coefficients (C_L , C_D , and C_M) and the tip bending deflections are compared to experimental results obtained by Garg et al. ([14]). Numerical results concur with

*Corresponding author

 jacques-andre.astolfi@ecole-navale.fr (J.A. Astolfi)

ORCID(s): 0000-0003-1002-0243 (J.A. Astolfi)

measured values for both the baseline and the optimized hydrofoils across a wide range of lift conditions.

In order to control lift generated by hydrofoils on boats, Giovannetti et al. [15] have numerically and experimentally analysed hydrofoil geometry designed to reduce the lift coefficient passively by increasing the flow velocity. This study was achieved through the use of wind tunnel experiments including displacements measurements, which concurred with the numerical results. They found that twist deformations resulted in a reduction in the effective angle of attack by 30% at higher flow velocities, which significantly reduced the foil's lift and drag.

The French Naval Academy Research Institute (IRENav) is interested in the study of deformed hydrofoils, their responses and enlarging their operating domain. Experimentally, the Fluid-Structure Interaction has been investigated by studying the structural response of a flexible lightweight hydrofoil undergoing various flow conditions including cavitating flow by Lelong et al. [21], [20]. An optimization of design and elastic characteristics of a hydrofoil equipped with deformable elements providing flexibility to the trailing edge was developed by Sacher et al. [24]. In their study, Arab et al. [2] analyzed experimentally and numerically the effect of an imposed internal pressure of a compliant composite hydrofoil. It is shown that pressure driven compliant composite structure allows to enlarge the operational domain of the compliant hydrofoil. Also, they found that cavitation can be controlled to some extent by changing only the internal pressure for a given angle of attack and a given inflow velocity. Vanilla et al. studied the fluid-structure interaction effect of bend twist coupling on hydrodynamic performance ([26]). They developed numerical approaches based on the FSI coupling algorithm and they compared the results to experimental ones obtained in the hydrodynamic tunnel.

Research studies begin to focus on the effect of the geometric parameters of hydrofoils in order to enlarge their non-cavitation domain. Ladino ([19]) conducted a numerical study using XFOIL software to investigate the effect of geometric parameters of NACA 4 series profiles on the cavitation characteristics. He evaluated the effect of camber percentage, camber location and maximum thickness. He also analyzed the effect of trailing edge deflection on the cavitation bucket. Results show that increase of thickness enlarges the non-cavitation domain. The same remark is noted for camber increment, especially at high angles of attack. Simulations show that the increasing camber and trailing edge deflection induce to the non cavitation bucket to move to high lift zone. In another study, the adverse effects of cavitation and roughness are taken into account by Sun et al. ([25]). They developed an algorithm to optimize geometric parameters of a NACA 2415 in order to affect lift and drag coefficient as well as the minimum pressure coefficient. Other studies are based on the optimization of the propeller geometry as the work of Gaggero et al. ([10]). Their study aimed at evaluating the performance of propellers selected by a genetic optimization algorithm including cavitation criteria.

The present paper presents an experimental and numeri-

cal study where the effect of leading and trailing edge deflections of a hydrofoil is investigated. The effect of the leading and trailing edge flaps on hydrodynamic performance is predicted using Xfoil software. Then, four hydrofoils taking advantage of design solution based on 3D printing at moderate cost compared to the high cost usual Inox steel manufacturing and tested in the cavitation tunnel.

The paper describes the experimental setup, the numerical computations and presents the main results.

2. Experimental setup

Experiments are carried out in the cavitation tunnel at IRENav (Fig. 1). The tunnel test section is 1 m length with a square section of 0.192 m side. The inflow velocity ranges between 0.5 and 15 m/s. The pressure in the tunnel test section ranges between 0.1 bar and 3 bar to control the cavitation which is given by a cavitation number defined by equation 1 and the measured turbulence intensity in the test section is 2% at 5 m/s. This cavitation number can therefore be compared to the opposite of pressure coefficient $-C_{pmin}$ defined as the minimum of pressure coefficient (equation 2).

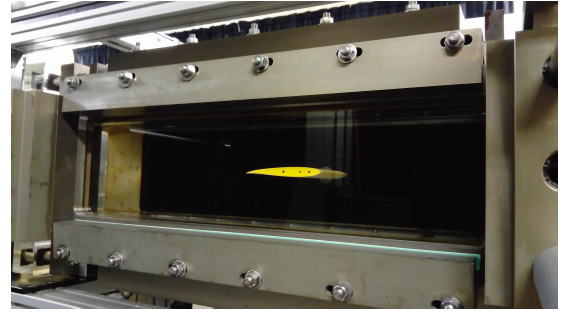


Figure 1: Hydrodynamic tunnel test section at IRENav with the NACA 0012 profile clamped on the opposite vertical wall.

$$\sigma = \frac{P_{ref} - P_v}{\frac{1}{2}\rho V^2} \quad (1)$$

$$C_p = \frac{P - P_{ref}}{\frac{1}{2}\rho V^2} \quad (2)$$

Where P_{ref} is the reference pressure in the test section, P_v is the vapor pressure at the water temperature, P is the local pressure, V is the inflow velocity, and ρ is the water density. Thus, when $\sigma < -C_{pmin}$, that is to say when $P < P_v$, cavitation is expected to appear in the flow at the point where the pressure coefficient is the lowest.

Four hydrofoils are manufactured using an additive manufacturing process based on 3D printing techniques (PLA material) and tested in the hydrodynamic tunnel at IRENav. The reference one is a symmetrical NACA 0012 and the others have a difference in the flap deflection angles and the rotating position. The different angles involved are described in Fig. 2. α is the angle of incidence, γ is the angle of the leading edge flap and β is the angle of the trailing edge flap.

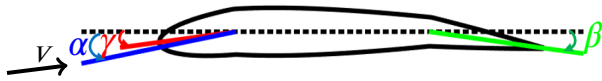


Figure 2: Schematic diagram of the different angles: angle of incidence (α), angle of the leading edge flap (γ) and angle of the trailing edge flap (β).

Figure 3 shows the four hydrofoil geometries used in this study. One of the hydrofoils has a leading edge flap at 20% c with the deflection angle of $\gamma = 3^\circ$, the second one has a trailing edge flap at 70% c with the deflection angle of $\beta = 5^\circ$ and the last one has the two flaps: leading edge flap at 20% c with the deflection angle of $\gamma = 3^\circ$ and trailing edge flap at 70% c with the deflection angle of $\beta = 5^\circ$. These hydrofoils have the same chord and span as the reference NACA 0012.

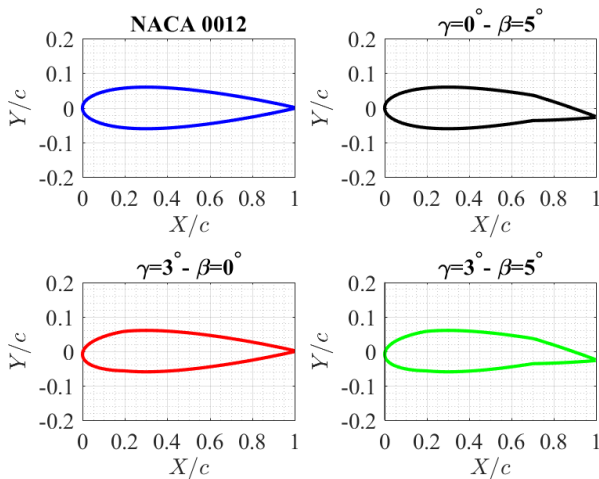


Figure 3: Reference NACA 0012 profile studied and hydrofoils sections with different flaps.

Hydrofoils are mounted in the test section using a new system developed in the institute which is named fairing system (support beam). To measure the components of the hydrodynamic forces, hydrofoils are mounted on an axis of rotation at $X/c = 0.25$. The axis of rotation is made of stainless steel to assess the stiffness of the structure of the hydrofoil (Fig. 6). The axis of rotation has a rectangular form and is fastened into the hydrodynamic balance, secured by a tight fitted key/nut system. Then the fairing (Fig. 5) corresponding to the different geometries are slide on the beam (Fig. 4). The beam is mounted to the balance by the mean of a bolted cylinder (Fig. 6). This mounting procedure assure the minimum disturbance of the setting of the hydrodynamic balance.

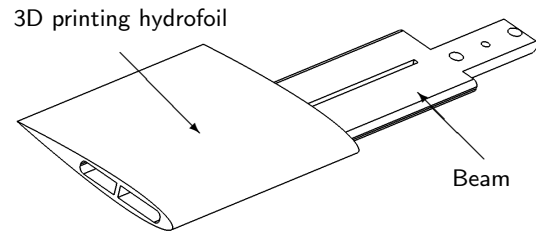


Figure 4: CAD of NACA 0012 with hydrofoil fairing system.



Figure 5: 3D printing NACA 0012 with fairing system.

In the aim to control transition problems, a roughness layer was set on the upper and lower hydrofoils surfaces at 5% c from the leading edge.

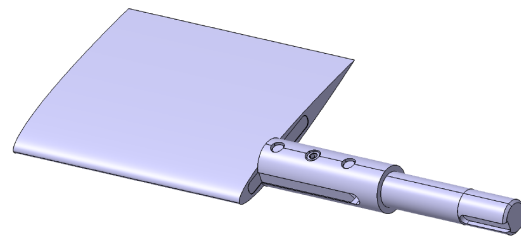


Figure 6: CAD of NACA 0012 profile with traditional mounting system.

2.1. Hydrodynamic balance

Measurement of hydrodynamic forces is performed using a hydrodynamic balance at various conditions of angle of attack. The 5-components hydrodynamic balance has a range up to 1700 N for the lift force, 180 N for the drag and 43 Nm for the pitching moment. It is fixed into a supporting frame, mounted on bearings (Fig. 7), and driven in rotation by a Baldor motor. The stepper motor allows for 600 000 impulses per turn on 360°, meaning a resolution of 0.0006°. The foil is fastened into the balance, secured by a tight fitted key/nut system [23]. As the test section is horizontal, the geometric 0° angle of attack of the hydrofoil is visually controlled using the water surface at mid height of the test section when filling the tunnel. Also, as the first hydrofoil is symmetric, the zero-lift angle is used to set the reference angle of attack.

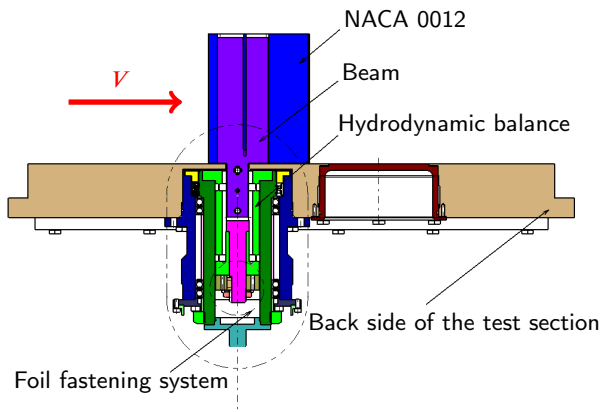


Figure 7: Overview from top of the mechanical set-up of the hydrodynamic balance.

2.2. Cavitation

The cavitation is visually observed under stroboscopic light. The inception condition is determined by increasing the angle of attack at a constant cavitation number until cavitation appeared. It consists in determining the angles and the lift coefficients for which cavitation occurred suction sides for a constant cavitation number. The cavitation inception is considered when an organized spanwise cavitation pattern is visually observed along a significant portion of the leading edge. For low cavitation numbers, typically lower than 1.5, the inception angle was determined until the first bubbles were visually detected on the suction side.

This visual technique used in the lab for the best 5 years and have proven not to depend of the user.

2.3. Flow condition and uncertainties

Measurement of hydrodynamic forces is performed using a hydrodynamic balance at various conditions of angle of attack at an inflow velocity of 6.67 m/s corresponding to a Reynolds number of 10^6 . Velocity and pressure measurements uncertainties are based on the accuracy of the pressure sensors. The latter is about 0.04 bar . About measurements of hydrodynamic forces and from the document provided by the manufacturer of the hydrodynamic balance, the uncertainties are about $\pm 1.02 \text{ N}$ for the lift, $\pm 0.324 \text{ N}$ for the drag and $\pm 0.26 \text{ N.m}$ for the pitching moment.

3. Numerical approach

The numerical study consists in 2D simulations to investigate the effect of leading and trailing edges deflections on the hydrodynamic performances.

Hydrofoils shapes are plotted using a direct foil design menu of Xfoil, which allows us to define the leading and trailing edges deflections and the rotating flaps positions. After, the flow model of the Xfoil solver is used to evaluate the hydrodynamic performances. The flow model is based on the coupling between a panel method and a boundary layer model. More details about Xfoil are given in [7]. The panel method speeds-up flow calculations as compared

to finite volume method.

Simulations are carried out for a Reynolds number of 10^6 and different angles of attack.

4. Results and discussion

4.1. Numerical results

The effect of the leading and trailing edges deflection angles is predicted using Xfoil software. Figure 8 illustrates the numerical lift coefficients of the different hydrofoils. As expected the trailing edge flap increases the lift coefficient of the hydrofoil. At the opposite, the leading edge deflection angle has very little effect on the lift coefficient. For the same angle of attack, the trailing edge flap increases the lift coefficient of about $\Delta C_L = 0.35$. When, the same operating point $C_L = 0.5$ is considered, the trailing edge $\beta = 5^\circ$ decreases the angle of attack from 4.48° to 1.35° ($\Delta\alpha = 3.13^\circ$). Results are consistent with the hydrodynamic tendencies.

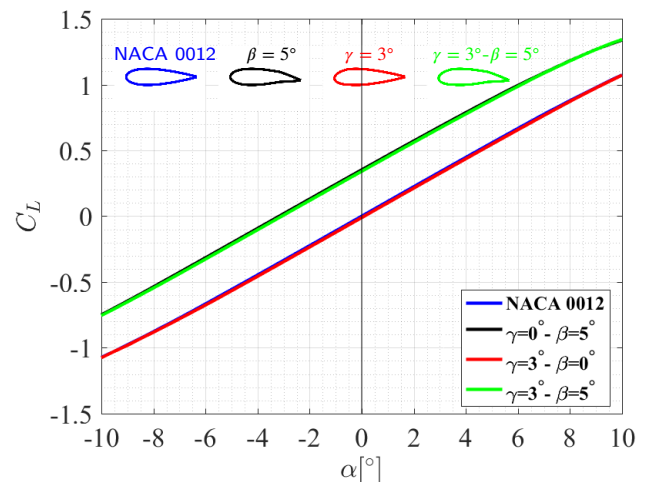


Figure 8: Effect of the leading edge and trailing edge flaps on the computed lift coefficient evolution as a function of the angle of attack, $Re = 10^6$.

The effect of the flaps deflections on the cavitation inception is also predicted using Xfoil analysis using the criteria ($-C_{pmin} = \sigma$). Figure 9 shows the lift coefficient versus the opposite of the minimum pressure coefficient ($-C_{pmin}$) of the four hydrofoils.

Flaps deflection has a direct influence on the theoretical cavitation inception, particularly for lift coefficients larger than 0.075. It is found that the leading and trailing edges deflections enlarge the non-cavitation domain. It is shown that the flap deflection makes the cavitation bucket to shift up. For low lift coefficients, the trailing edge flap is sufficient to delay the cavitation inception. For the high lift coefficients, the leading edge flap is necessary to enlarge the non-cavitation domain and it provides a significant gain.

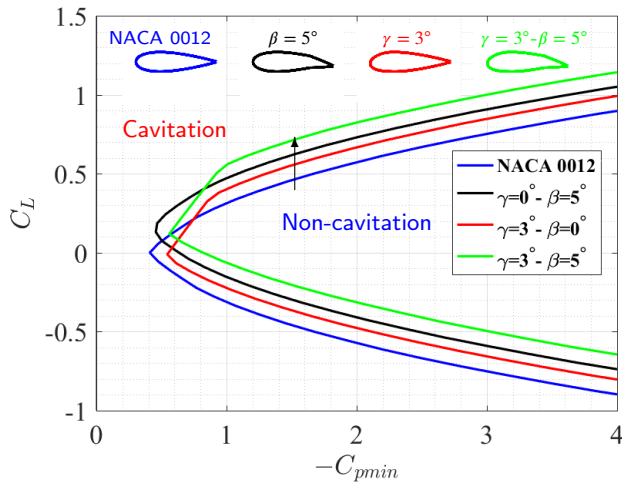


Figure 9: Numerical cavitation bucket of NACA 0012, NACA 0012 with leading edge flap, NACA 0012 with trailing edge flap and NACA 0012 with leading and trailing edge flaps, $Re = 10^6$.

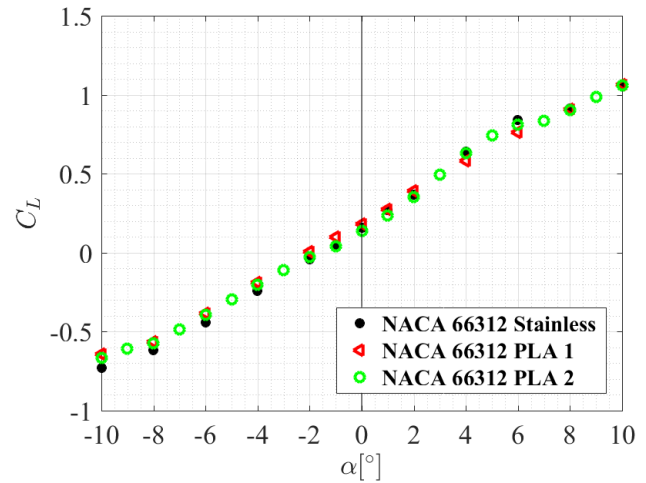


Figure 10: Experimental lift coefficients of both NACA 66312 hydrofoil made of stainless steel and PLA, $Re = 5.33 \times 10^5$.

4.2. Experimental validation of the fairing system

Hydrodynamic coefficients measured on the PLA-NACA 66312 hydrofoils mounted using a fairing system are compared to those measured on the stainless steel NACA 66312 hydrofoil mounted using the traditional mounting system. This type of profile is often used for the propeller blades in industry and widely studied at IRENav ([22] and [8])

The experimental evolution of the lift and drag coefficients as a function of the angle of attack are presented respectively in Fig. 10 and Fig. 11. They summarize the experimental coefficients measured on the hydrofoil made of stainless steel and on the hydrofoils fairing manufactured using 3D printer technique.

It is shown that the lift coefficient measured on the stainless steel profile has the same trend as the one measured on hydrofoils manufactured in 3D printing. The same remark is obtained for the drag coefficient. During this analysis, the maximum difference between the experimental lift coefficients is about 0.087. This difference was noted at $\alpha = -10^\circ$ angle of incidence between the stainless steel profile and the PLA 1 profile. For the drag coefficient, the maximum difference is obtained for the same angle of incidence ($\alpha = -10^\circ$) and it was lower than 0.0304. Far from the stall area, the maximum difference between the C_L measured on the hydrofoils made of the stainless steel and PLA 1 is about 0.076 noted at $\alpha = 6^\circ$.

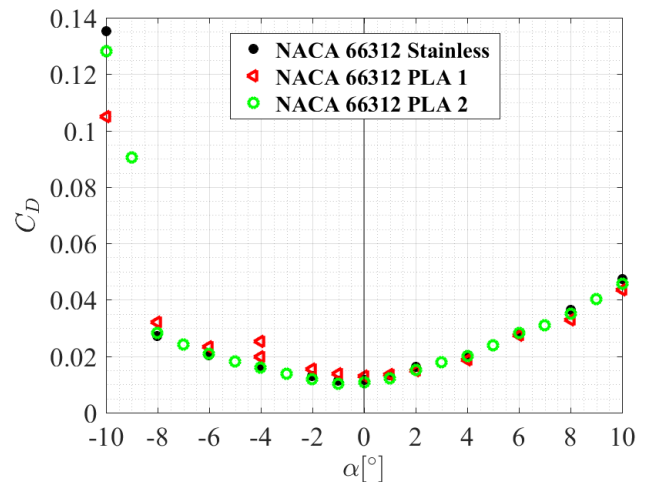


Figure 11: Experimental drag coefficients of both NACA 66312 hydrofoil made of stainless steel and PLA, $Re = 5.33 \times 10^5$.

The cavitation inception on the NACA 66312 hydrofoils made using 3D printer technique is compared to the cavitation inception obtained on the same type of hydrofoil made of stainless steel. Various measurement campaigns were carried out at 5.33×10^5 Reynolds number. The experimental cavitation buckets are presented in Fig. 12.

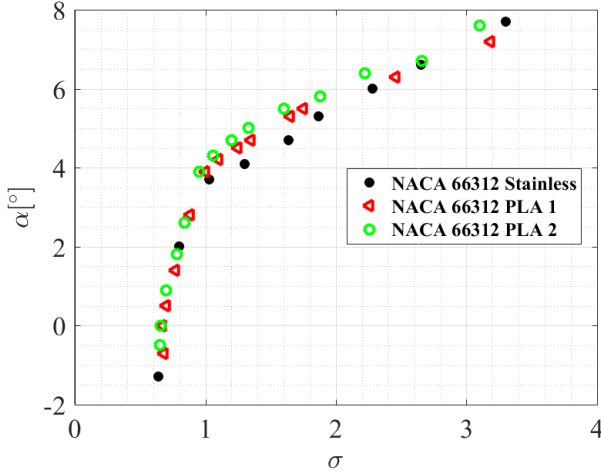


Figure 12: Experimental cavitation buckets of NACA 66312 profiles made of stainless steel and of PLA, $Re = 5.33 \cdot 10^5$.

The conditions of cavitation inception on the PLA hydrofoils suction side are similar to those of cavitation inception on the stainless steel hydrofoil. However, the values are lower for the stainless steel hydrofoil. The order of maximum difference between the angles of the cavitation inception on the stainless steel hydrofoil and the hydrofoil made of PLA is about $\Delta\alpha = 0.8^\circ$ noted at the cavitation numbers $\sigma = 1.6$ and $\sigma = 1.3$. This difference can be explained by the step of incidence $\Delta\alpha$ chosen, thus the fluctuations of speed and pressure in the test section. We conclude that the 3D printed faring can be used for cavitation experimental campaign.

4.3. Experimental results of the effect of flap on hydrodynamic performances

The 3D printed hydrofoils are studied in cavitation tunnel at IRENav. For a Reynolds number of 10^6 , the lift coefficients measured using the hydrodynamic balance are presented in Fig. 13. These experimental results are compared to the numerical ones obtained from the numerical study. The experimental results for the four hydrofoils fit with the numerical ones showing the ability of Xfoil to simulate the hydrodynamic performance (coefficients). Figure. 14 presents the experimental and numerical lift coefficients of the four hydrofoils.

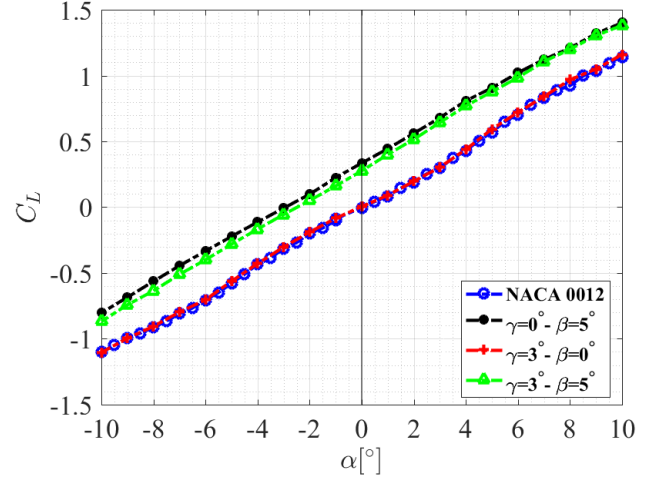


Figure 13: Experimental lift coefficients of the four hydrofoils, $Re = 10^6$.

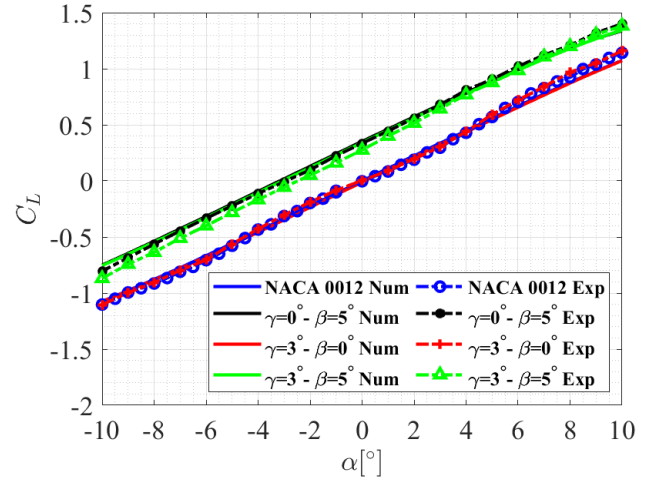


Figure 14: Experimental and numerical lift coefficients of the four hydrofoils, $Re = 10^6$.

For each hydrofoil and various cavitation numbers, cavitation inception and desinence are investigated. They are compared to the theoretical bucket predicted using Xfoil as presented in Fig. 15 which summarizes the conditions for cavitation inception and desinence on the hydrofoils surfaces. The abscissa denotes the cavitation number when the ordinate denotes the lift coefficient for which cavitation is visually detectable. A good agreement is found between numerical and experimental results, particularly for low lift coefficients and cavitation desinence. For $C_L > 0.6$ the experimental cavitation bucket discard from the numerical ones. An hysteresis between the cavitation inception and desinence for the same cavitation number is observed. This hysteresis means that the pressure required for the cavitation inception must be less than the pressure required for the cavitation desinence ([3]). Figure. 16 illustrates the observed cavitation, located at the leading edge, on a 3D printed hydrofoil.

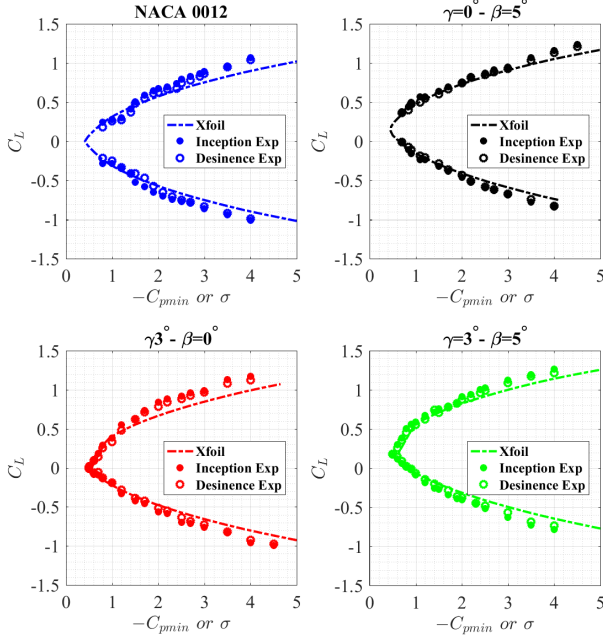


Figure 15: Experimental cavitation inception and desinence compared to the numerical ones of the NACA 0012 and hydrofoils with flaps, $Re = 10^6$.

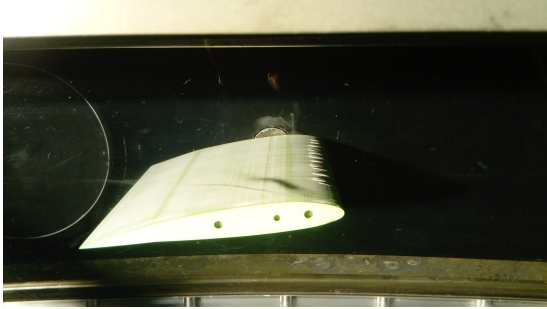


Figure 16: Experimental cavitation inception on the hydrofoil surface, $Re = 10^6$, PLA 3D printed fairing hydrofoils, $\gamma = 3^\circ$, $\beta = 5^\circ$.

To highlight the effect of leading and trailing edge flaps, the variation of cavitation number for the same operating point is extracted. For the same lift coefficient $C_L = 0.5$, the non-cavitation domains enlarged from about $\Delta\sigma = 0.7$ (Fig. 17).

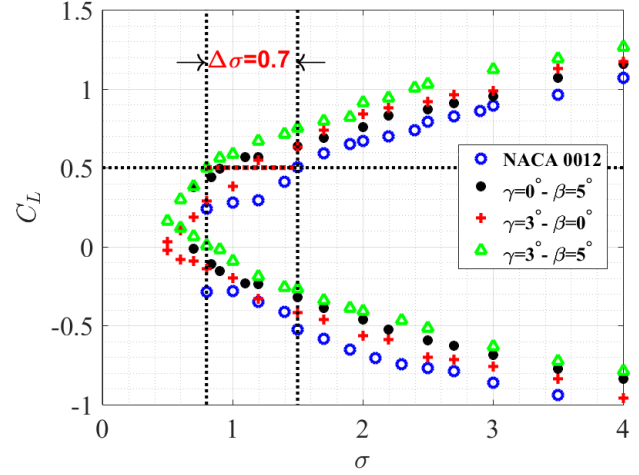


Figure 17: Effect of the flaps on the experimental cavitation buckets of the NACA 0012.

This enlargement of the non-cavitation domain is well predicted by the numerical model.

4.4. Effect of the trailing edge flap shape on the hydrodynamic performance

In aerodynamics, several studies have been carried out in order to define the shape of the trailing edge flap which allows the same deflection as the traditional flap, but which eliminates the discontinuities in the pressure coefficient distribution. To define the camber line of the morphing trailing edge, Abdessemed et al. ([1]) used a third order polynomial that is given by the equation 3 and they compared the results of the morphed airfoil to those of a flapped airfoil. It was observed that the morphed airfoil produced a higher lift/drag ratio than the flapped one.

The same equation for the camber line of the trailing edge flap was used by Hunsaker et al. ([16]). The objective is to suppress the discontinuous camber line slope at the hinge point of the traditional flap. They have shown that the contribution of this type of flap can be 33 to 50% more than that of the traditional flap.

The equation 3 represents the third order polynomial which defines the camber line of the morphing part of the hydrofoil (flap). This equation is added to the equation of the thickness distribution of a four-digit NACA profile which is defined in equation 4.

$$Y_c = \begin{cases} 0, & 0 \leq X \leq X_s \\ -w_{te} \frac{(X - X_s)^3}{(1 - X_s)^3}, & X \geq X_s \end{cases} \quad (3)$$

With Y_c is the camber line of the morphing part of the hydrofoil, X is the non-dimensional chord, X_s chordwise start location of morphing, w_{te} is the value of maximum deflec-

tion at the trailing edge.

$$Y_t = (th/c) \begin{pmatrix} 0.2969\sqrt{X} - 0.1260X - 0.3516X^2 \\ +0.2843X^3 - 0.1510X^4 \end{pmatrix}. \quad (4)$$

Y_t is the hydrofoil thickness distribution and th is the non-dimensional hydrofoil thickness ($th = 0.12$ for NACA 0012).

Figure 18 represents the geometry of the symmetrical hydrofoil (NACA 0012), the geometry of the hydrofoil with the morphed trailing edge flap defined by a third order polynomial (equation 3) and the geometry of the NACA 0012 hydrofoil with a traditional flap. In this study, the deflection of the two flaps is about 5° and the hinge point or the rotation axis of the flap is located at 70% of the chord. The shapes of the trailing edge flaps are shown in Fig. 19. The latter shows that the flap with a parabolic shape eliminates the discontinuity at the hinge point, assuring therefore a better surface continuity condition.

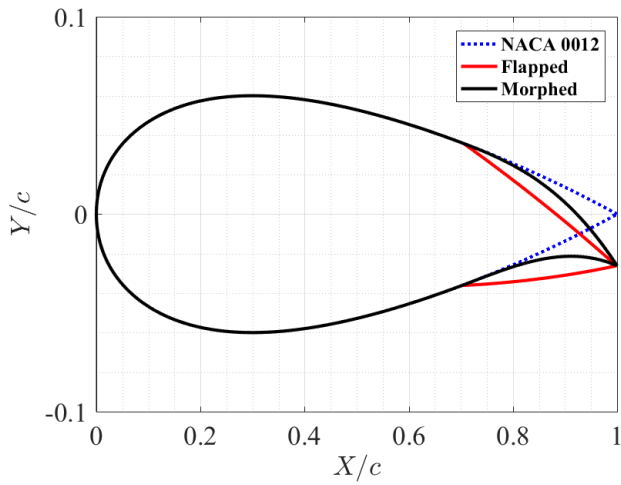


Figure 18: The geometries of the symmetrical hydrofoil and the hydrofoils with the traditional and parabolic flaps, $\beta = 5^\circ$.

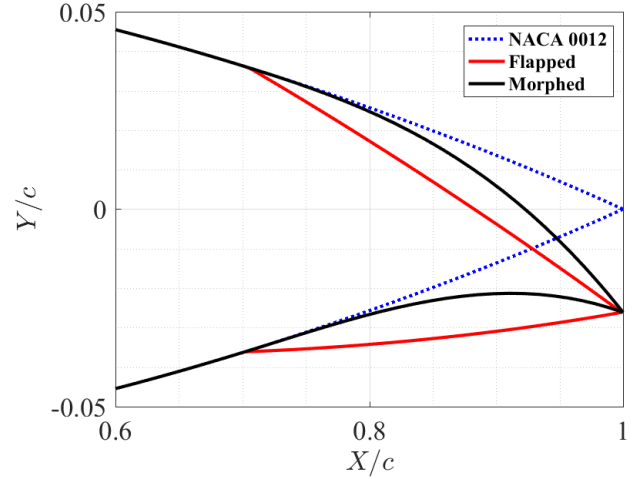


Figure 19: The geometries of the trailing edges of the symmetrical hydrofoil and the traditional and parabolic flaps, $\beta = 5^\circ$.

The different hydrofoils presented previously are numerically analyzed using Xfoil at the same flow conditions ($Re = 10^6$, $N_{crit} = 9$, $X_{tr} = 0.05$ and $-10^\circ < \alpha < +10^\circ$). The lift coefficients are presented in Fig. 20. At $\alpha = 0^\circ$, the traditional flap at 5° allows the increase of the C_L about 0.329, but the parabolic flap allows a better increase of the lift coefficient. The last one is about 0.45 compared to the hydrofoil without flap and it is about 0.12 when it is compared to the hydrofoil with the traditional flap at the same trailing edge deflection angle.

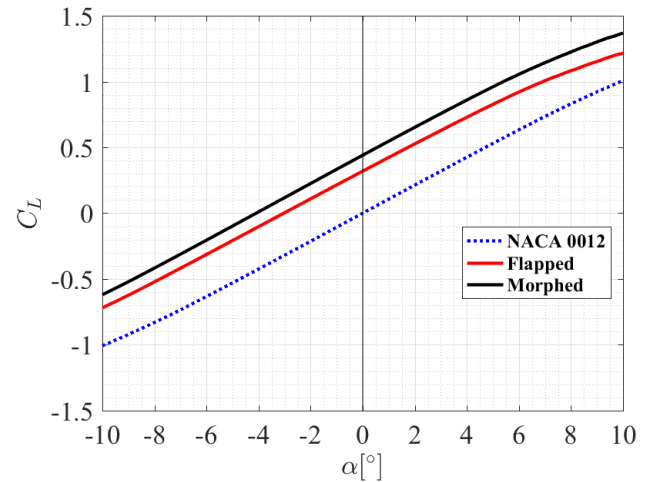


Figure 20: Lift coefficients as a function of the angle of incidence of the NACA 0012 hydrofoil, the hydrofoil with a traditional trailing edge flap at 5° and the hydrofoil with a parabolic trailing edge flap, $Re = 10^6$.

The trailing edge flaps have also an advantage on the C_L/C_D ratios of the initial hydrofoil. The effects of the traditional and parabolic trailing edge flaps on the C_L/C_D ratios are presented in Fig. 21. It is observed that the C_L/C_D of the hydrofoil with the parabolic trailing edge flap is higher

than the C_L/C_D of the hydrofoil with the traditional flap.

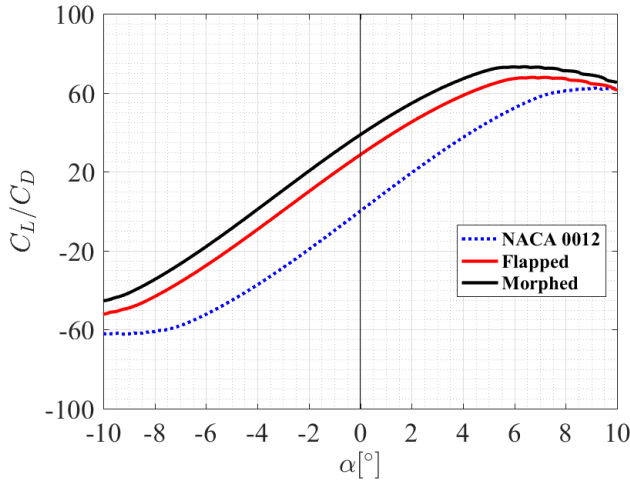


Figure 21: C_L/C_D as a function of the angle of incidence of the NACA 0012 hydrofoil, the hydrofoil with a traditional trailing edge flap at 5° and the hydrofoil with a parabolic trailing edge flap, $Re = 10^6$.

In this part, the effect of the trailing edge flap shape on the cavitation bucket of the initial hydrofoil (NACA 0012) is analyzed. The lift coefficient versus the opposite of the minimum pressure coefficient ($-C_{pmin}$) for the three hydrofoils are presented in Fig. 22. It is shown that the traditional flap enlarges the non-cavitation domain for $C_L > 0.067$ and the parabolic flap for $C_L > 0.107$. For a lift coefficient greater than 0.16, the morphed flap shifts up the cavitation bucket with no significant effect on the area of the bucket itself. For an operating point characterized by a $C_L = 0.5$, the hydrofoil with a traditional trailing edge flap decreases the cavitation number about 0.581 as it is compared to the cavitation number of the hydrofoil without flap. The gain at $C_L = 0.5$ of the parabolic flap on cavitation number is $\Delta\sigma = 0.213$ of the flapped hydrofoil, representing a total gain of 0.794 with the NACA 0012.

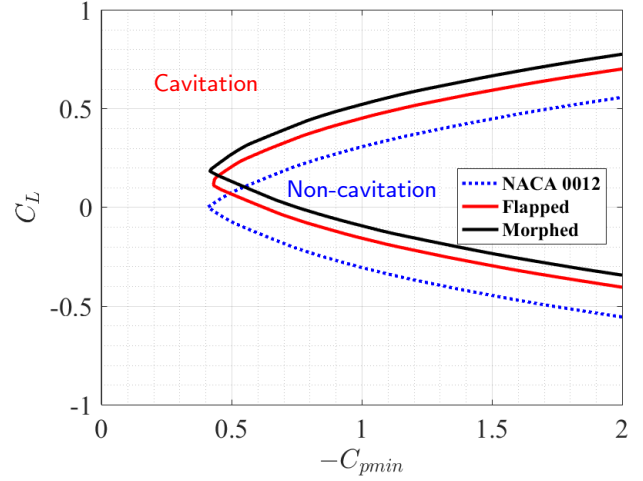


Figure 22: Predicted cavitation buckets of the hydrofoil without flap, hydrofoil with a traditional trailing edge flap at 5° and the hydrofoil with a parabolic trailing edge flap, $Re = 10^6$, $N_{crit} = 9$ and $X_{tr} = 0.05$.

At the operating point $CL = 0.5$ and the same flow conditions ($Re = 10^6$, $N_{crit} = 9$ and $X_{tr} = 0.05$), the pressure coefficient distributions around the three hydrofoils are plotted in Fig. 23. A pressure spike at the hinge point is caused by the discontinuity in the camber line slope of the traditional flap. This large pressure gradient can induce flow separation at the hinge point. The parabolic flap suppresses the pressure spike at the hinge point, but enlarges the pressure gradient near the hydrofoil trailing edge, which can induce flow separation in this region.

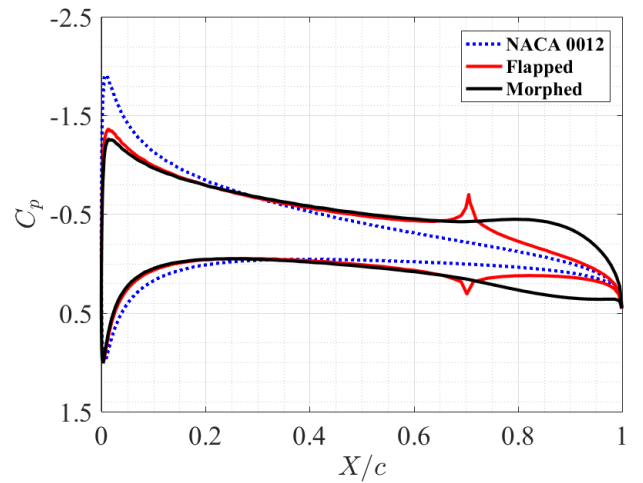


Figure 23: Pressure coefficient distribution calculated along the surface of the NACA 0012 without flap, with the traditional trailing edge flap and with the parabolic trailing edge flap at $C_L = 0.5$, $\beta = 5^\circ$, $Re = 10^6$, $N_{crit} = 9$ and $X_{tr} = 0.05$.

In the last part, we experimentally compared the results of the morphing trailing edge by manufacturing a hydrofoil with a parabolic flap using a 3D printer technique. The ex-

periments are carried out in the hydrodynamic tunnel at the IRENav with an inflow condition of $Re = 10^6$ and different angles of attack. The lift and drag coefficients are measured using the hydrodynamic balance. Results are compared to the hydrofoil with a traditional flap at 5° .

Figure 24 shows the experimental lift coefficients measured on the symmetrical hydrofoil (NACA 0012), the hydrofoil with a traditional flap ($\beta = 5^\circ$) and the hydrofoil with a parabolic trailing edge flap (equation 3). These experiments highlight the effect of the trailing edge flap on the lift coefficient of the hydrofoil without flap. From the Fig. 24, it is clearly shown that the flap camber significantly increases the lift coefficient of the hydrofoil at the studied conditions.

It is noted that for the same deflection angle ($\beta = 5^\circ$), the parabolic trailing edge flap produces a higher lift coefficient with an increase in the lift coefficient of about 11% at $\alpha = 5^\circ$ as compared with the C_L of the flapped hydrofoil.

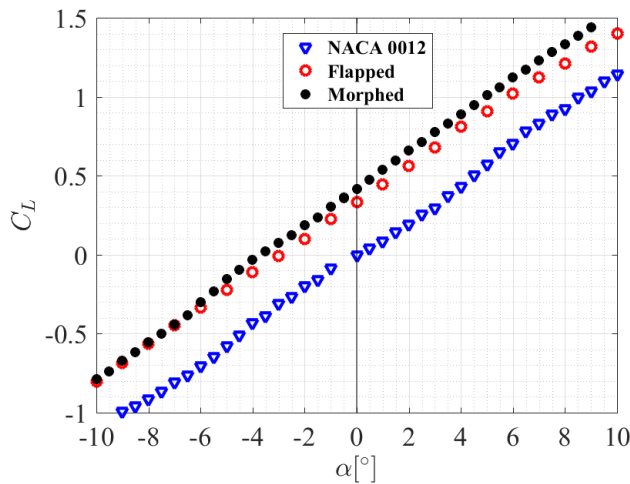


Figure 24: Lift coefficient experimentally measured on the NACA 0012 without flap, with the traditional trailing edge flap and with the parabolic trailing edge flap, $Re = 10^6$.

Figure 25 illustrates the experimental lift-to-drag ratio. The morphed and the flapped hydrofoils have their maximum C_L/C_D shifted to the left due to the flap. At low C_L ($\alpha -10^\circ$ to 0°) the morphed has a better performance than the flapped when the inverse tendency is observed at high lift. The morphed hydrofoil has a clear advantage on drag at low C_L

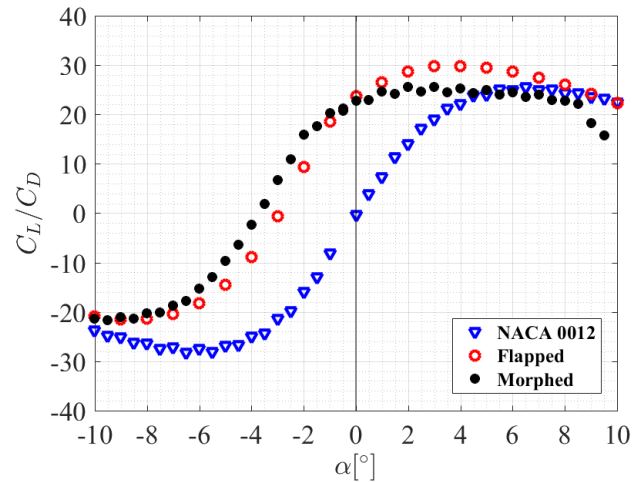


Figure 25: Experimental hydrodynamic lift to drag ratio versus angle of attack for initial hydrofoil and hydrofoils with morphed and flapped trailing edges, $Re = 10^6$, $\beta = 5^\circ$.

Figure 26 summarizes the cavitation buckets of the symmetrical hydrofoil, flapped and morphed hydrofoils. These results confirm the behavior that was predicted previously using Xfoil. The cavitation bucket moves up for the hydrofoils with trailing edge flaps. The flapped and the morphing trailing edges enlarge the non-cavitation domain of the initial hydrofoil for the positive lift coefficient. The hydrofoil with a parabolic trailing edge flap pushes the cavitation further away than the hydrofoil with a traditional flap. For example, at $C_L = 0.5$, the morphed hydrofoil gives a variation of cavitation number of 0.34 as compared to the flapped hydrofoil.

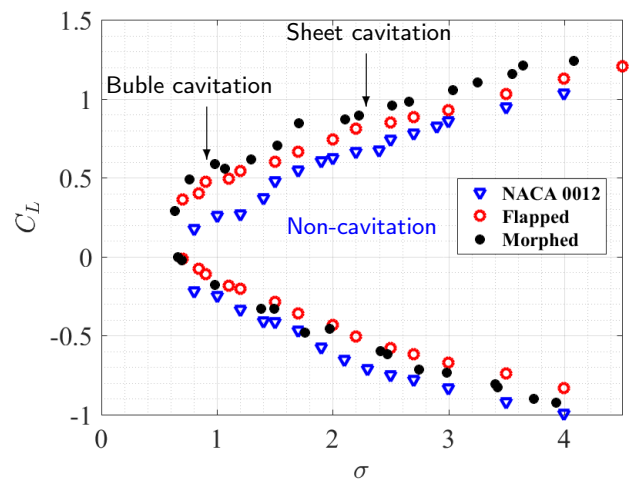


Figure 26: Experimental cavitation buckets of the NACA 0012 without flap, with the traditional trailing edge flap and with the parabolic trailing edge flap, $Re = 10^6$.

5. Conclusions

In this paper, an experimental and a numerical study have been presented in order to assess the effect of the leading and trailing edge flaps on the hydrodynamic performances of a hydrofoil.

Firstly, the effect of the leading and trailing edge flaps deflection angles on the hydrodynamic coefficients and cavitation bucket is analyzed at $Re = 10^6$ using Xfoil software. Then, the effect of the trailing edge flap shape on the hydrodynamic performance is studied. The hydrodynamic coefficients of a hydrofoil with a traditional trailing edge flap at $\beta = 5^\circ$ are compared to the same hydrofoil with a parabolic trailing edge flap.

Experimentally, four hydrofoils are manufactured using 3D printer technique and tested in the hydrodynamic tunnel at IRENav. The first hydrofoil is a reference one NACA 0012 without flaps, the second hydrofoil has a trailing edge flap of $\beta = 5^\circ$ at $70\%c$, the third one has a leading edge flap of $\gamma = 3^\circ$ at $20\%c$ and the hydrofoil has a leading and trailing edge flaps of $\gamma = 3^\circ$ and $\beta = 5^\circ$ respectively. Hydrodynamic forces are measured using the hydrodynamic balance. To analyze the cavitation inception, the experimental cavitation buckets are plotted for the different hydrofoils and compared to the theoretical ones predicted by Xfoil model.

Xfoil simulations show that the trailing edge deflection angle increases the lift coefficient, contrary to the leading edge which has not an effect on the hydrodynamic forces. It is also noted that the leading and trailing edge deflections enlarge the non-cavitation domain of hydrofoil NACA 0012. Results of these simulations are compared to the experimental ones obtained in the cavitation tunnel at IRENav. It is concluded that the numerical fit well the experimental ones.

The shape of the trailing edge flap affects the hydrodynamic coefficients and the cavitation bucket. The hydrofoil with a parabolic flap gives more lift than the traditional flap and can enlarge the non-cavitation domain to some extent of the lift coefficients. This study also shows that the parabolic trailing edge flap suppresses the pressure spike at the hinge point caused by the traditional trailing edge flap. The results of these simulations are confirmed by the experimental test.

Nomenclature

| | |
|-----------|--|
| α | angle of attack [$^\circ$]. |
| β | trailing edge deflection [$^\circ$]. |
| γ | leading edge deflection [$^\circ$]. |
| ρ | fluid density [kg/m^3]. |
| σ | cavitation number: $\sigma = \frac{P-P_v}{\frac{1}{2}\rho V^2}$ [-]. |
| c | hydrofoil chord [m]. |
| C_D | drag coefficient: $C_D = \frac{D}{\frac{1}{2}\rho V^2 s}$ [-]. |
| C_L | lift coefficient: $C_L = \frac{L}{\frac{1}{2}\rho V^2 s}$ [-]. |
| C_p | pressure coefficient: $C_p = \frac{P-P_{ref}}{\frac{1}{2}\rho V^2}$ [-]. |
| D | drag force [N]. |
| e | hydrofoil span [m]. |
| h | immersion of the hydrofoil [m]. |
| L | lift force [N]. |
| P | pressure [bar]. |
| Re | Reynolds number: $Re = Vc/\nu$ [-]. |
| s | hydrofoil planform [m^2]. |
| V | inflow velocity [m/s]. |
| X, Y, Z | foil coordinates [m]. |
| ν | kinematic viscosity [m^2/s]. |

Acknowledgments

The authors would like to thank the technical staff of the French Naval Academy Research Institute for their support to this study.

References

- [1] Abdessemed, C., Yao, Y., Narayan, P., Bouferrouk, A., 2020. Unsteady parametrization of a morphing wing design for improved aerodynamic performance .
- [2] Arab, F.M., Augier, B., Deniset, F., Casari, P., Astolfi, J.A., 2019. Morphing hydrofoil model driven by compliant composite structure and internal pressure. *Journal of Marine Science and Engineering* 7, 423.
- [3] Astolfi, J.A., Dorange, P., Billard, J.Y., Tomas, I.C., 2000. An experimental investigation of cavitation inception and development on a two-dimensional eppiler hydrofoil. *J. Fluids Eng.* 122, 164–173.
- [4] Barbarino, S., Bilgen, O., Ajaj, R.M., Friswell, M.I., Inman, D.J., 2011. A review of morphing aircraft. *Journal of intelligent material systems and structures* 22, 823–877.
- [5] Brailovski, V., Terriault, P., Coutu, D., Georges, T., Morellon, E., Fischer, C., Bérubé, S.b., 2008. Morphing laminar wing with flexible extradors powered by shape memory alloy actuators, in: *Smart Materials, Adaptive Structures and Intelligent Systems*, pp. 615–623.
- [6] Dimino, I., Lecce, L., Pecora, R., 2017. *Morphing Wing Technologies: Large Commercial Aircraft and Civil Helicopters*. Butterworth-Heinemann.
- [7] Drela, M., 1989. Xfoil: An analysis and design system for low reynolds number airfoils, in: *Low Reynolds number aerodynamics*. Springer, pp. 1–12.
- [8] Ducoin, A., 2008. Etude expérimentale et numérique du chargement hydrodynamique des corps portants en régime transitoire avec prise en compte du couplage fluide structure. Ph.D. thesis. Nantes.
- [9] Ducoin, A., Astolfi, J.A., Sigrist, J.F., 2012. An experimental analysis of fluid structure interaction on a flexible hydrofoil in various flow regimes including cavitating flow. *European Journal of Mechanics-B/Fluids* , 63–74.

- [10] Gaggero, S., Gonzalez-Adalid, J., Sobrino, M.P., 2016. Design of contracted and tip loaded propellers by using boundary element methods and optimization algorithms. *Applied Ocean Research* 55, 102–129.
- [11] Garg, N., Kenway, G., Martins, J., Young, Y., 2016. High-fidelity hydrostructural optimization of a 3-d hydrofoil, in: *International Symposium on Transport Phenomena and Dynamics of Rotating Machinery*, Honolulu, HI, Apr, pp. 10–15.
- [12] Garg, N., Kenway, G.K., Martins, J.R., Young, Y.L., 2017. High-fidelity multipoint hydrostructural optimization of a 3-d hydrofoil. *Journal of Fluids and Structures* 71, 15–39.
- [13] Garg, N., Lyu, Z., Dhert, T., Martins, J., Young, Y.L., 2015. High-fidelity hydrodynamic shape optimization of a 3-d morphing hydrofoil. *Fourth International Symposium on Marine Propulsors*.
- [14] Garg, N., Pearce, B.W., Brandner, P.A., Phillips, A.W., Martins, J.R., Young, Y.L., 2019. Experimental investigation of a hydrofoil designed via hydrostructural optimization. *Journal of Fluids and Structures* 84, 243–262.
- [15] Giovannetti, L.M., Banks, J., Ledri, M., Turnock, S.R., Boyd, S.W., 2018. Toward the development of a hydrofoil tailored to passively reduce its lift response to fluid load. *Ocean Engineering* 167, 1–10.
- [16] Hunsaker, D.F., Reid, J.T., Joo, J.J., 2019. Geometric definition and ideal aerodynamic performance of parabolic trailing-edge flaps. *International Journal of Astronautics and Aeronautical Engineering* 4.
- [17] Jawahar, H.K., Ai, Q., Azarpeyvand, M., 2018. Experimental and numerical investigation of aerodynamic performance for airfoils with morphed trailing edges. *Renewable energy* 127, 355–367.
- [18] Kaul, U.K., Nguyen, N.T., 2018. Drag characterization study of variable camber continuous trailing edge flap. *Journal of Fluids Engineering* 140, 101108.
- [19] Ladino, A., 2011. Numerical study of cavitation characteristics of profiles for use in marine current turbines, in: *ASME International Mechanical Engineering Congress and Exposition*, pp. 863–868.
- [20] Lelong, A., Guiffant, P., Astolfi, J.A., 2016. An experimental analysis of the structural response of flexible lightweight hydrofoils in various flow conditions. *16th International Symposium on Transport Phenomena and Dynamics of Rotating Machinery*.
- [21] Lelong, A., Guiffant, P., Astolfi, J.A., 2018. An experimental analysis of the structural response of flexible lightweight hydrofoils in cavitating flow. *Journal of Fluids Engineering* 140, 021116.
- [22] Leroux, J.B., Coutier-Delgosha, O., Astolfi, J.A., 2005. A joint experimental and numerical study of mechanisms associated to instability of partial cavitation on two-dimensional hydrofoil. *Physics of fluids* 17, 052101.
- [23] Marchand, J.B., Astolfi, J.A., Bot, P., 2017. Discontinuity of lift on a hydrofoil in reversed flow for tidal turbine application. *European Journal of Mechanics-B/Fluids* 63, 90–99.
- [24] Sacher, M., Durand, M., Berrini, E., Hauville, F., Duvigneau, R., Le Maitre, O., Astolfi, J.A., 2018. Flexible hydrofoil optimization for the 35th america's cup with constrained ego method. *Ocean Engineering* 157, 62–72.
- [25] Sun, Z., Mao, Y., Fan, M., 2020. Performance optimization and investigation of flow phenomena on tidal turbine blade airfoil considering cavitation and roughness. *Applied Ocean Research*, 102463.
- [26] Vanilla, T.T., Benoit, A., Benoit, P., 2021. Hydro-elastic response of composite hydrofoil with fs. *Ocean Engineering* 221, 108230.
- [27] Weisshaar, T.A., 2013. Morphing aircraft systems: historical perspectives and future challenges. *Journal of aircraft* 50, 337–353.
- [28] Woods, B.K., Parsons, L., Coles, A.B., Fincham, J.H., Friswell, M.I., 2016. Morphing elastically lofted transition for active camber control surfaces. *Aerospace Science and Technology* 55, 439–448.
- [29] Young, Y.L., Motley, M.R., Barber, R., Chae, E.J., Garg, N., 2016. Adaptive composite marine propulsors and turbines: progress and challenges. *Applied Mechanics Reviews* 68, 060803.